Inorganic Chemistry

Article

pubs.acs.org/IC

Crystal Structure, Transport, and Magnetic Properties of an Ir^{6+} Compound $Ba_8Al_2IrO_{14}$

Lin Yang,[†,‡] Andrea Pisoni,[†] Arnaud Magrez,[§] Sergiy Katrych,[†] Alla Arakcheeva,[†] Bastien Dalla Piazza,[‡] Krunoslav Prša,[‡] Jaćim Jaćimović,[†] Ana Akrap,[∥] Jérémie Teyssier,[∥] László Forró,[†] and Henrik M. Rønnow*[,‡,⊥,#]

[†]Laboratory of Physics of Complex Matter, [‡]Laboratory for Quantum Magnetism, and [§]Crystal Growth Facility, Ecole Polytechnique Fédérale de Lausanne (EPFL), CH-1015 Lausanne, Switzerland

[∥]DPMC, University of Geneva, CH-1211 Geneva, Switzerland

[⊥]Neutron Science Laboratory, Institute of Solid State Physics (ISSP), University of Tokyo, Kashiwa, Japan

[#]Center for Emergent Matter Science (CEMS), RIKEN, Wako-shi, Japan

Supporting Information

ABSTRACT: The novel iridate $Ba_8Al_2IrO_{14}$ was prepared as single crystals by self-flux method, thereby providing a rare example of an all-Ir(VI) compound that can be synthesized under ambient pressure conditions. The preparation of all-Ir^{6+} iridate without using traditional high-pressure techniques has to our knowledge previously only been reported in $Nd_2K_2IrO_7$ and $Sm_2K_2IrO_7$. The monoclinic crystal structure (space group $C2/m$, No.12) is stable down to 90 K and contains layers of IrO_6 octahedra separated by Ba and AlO_4 tetrahedra. The material exhibits insulating behavior with a narrow band gap of ∼0.6 eV. The positive Seebeck coefficient indicates hole-like dominant charge carriers. Susceptibility measurement shows antiferromagnetic coupling with no order down to 2 K.

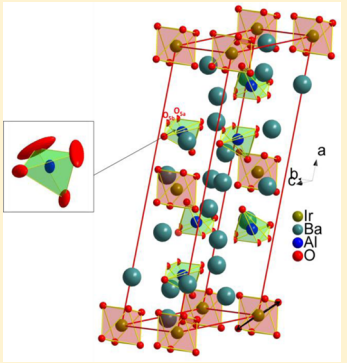

INTRODUCTION

Recently, there has been considerable interest in studying correlated 5d-electron transition metal oxides. Unlike 3d transition metal oxides, 5d materials were expected to be less correlated because of extended orbitals. Therefore, a tendency to metallic behavior was expected. However, experiments have shown that some compounds, such as $Sr_3Ir_2O_7$, Na_2IrO_3, and Ba_2NaOsO_6, show insulating behavior.[1−3] Some recent reports show that correlation effects could be important for the 5d insulating transition metal oxides.[4−6] One example is $Ba_3YIr_2O_9$,[7] which crystallizes in a hexagonal structure and transforms into a cubic structure under an applied pressure of 8 GPa at 1273 K; strong spin−orbit coupling (SOC) plays a crucial role in determining the magnetic and insulating properties of this system in both phases.

Iridium-based oxides are relatively unexplored, although they are expected to exhibit interesting physical properties. In the majority of iridium-based compounds Ir^{4+} is stabilized, and most of recent theoretical and experimental work has focused on the tetravalent iridates (Ir^{4+}). On the other hand, Ir^{5+} and Ir^{6+} can also be obtained under high oxygen pressure conditions, but little attention has been drawn to them.[8−12]

In this work we show the ambient-pressure synthesis and physical properties of a new all-Ir^{6+} iridate $Ba_8Al_2IrO_{14}$. The preparation of all-Ir^{6+} iridate without using traditional high-pressure techniques has to our knowledge previously only been reported in $Nd_2K_2IrO_7$ and $Sm_2K_2IrO_7$.[13]

EXPERIMENTAL SECTION

Synthesis. Single crystals of $Ba_8Al_2IrO_{14}$ were grown as unexpected byproducts in our attempt to synthesize $Ba_3Ir_2YO_9$ single crystals. In this process, single crystals of $Ba_8Al_2IrO_{14}$ were produced by reacting $BaCO_3$, IrO_2, and Y_2O_3 powder by self-flux method in Al_2O_3 crucible. The mixture of the powders with the ratio of $BaCO_3/IrO_2/Y_2O_3$ = 26:4:1 was heated for 2 h at 1250 °C and rapidly cooled to room temperature. After the reaction, small black single crystals were found to have a needlelike shape. The maximum dimensions were ∼0.5 mm in length and ∼0.1 mm in width (Figure 1). The needle axes coincide with the crystallographic b-axis. Grinding the black crystals produced brown power. The crystals are very sensitive to moisture. The chemical composition of the resulting compound was determined using an energy-dispersive X-ray detector (EDX, Oxford Instruments EDX X-MAX). The EDX analysis revealed the presence of Ba, Ir, and Al. We conclude that the raw materials reacted with the Al_2O_3 crucible to acquire Al. This conclusion was supported by inspection of the crucible after reaction, where the crystals could be seen to grow in needles away from the crucible wall. The EDX analysis suggested molar ratios Ba/Al/Ir of 80.1(7):10.3(5):9.6(10), but for these

Received: January 22, 2015

 © XXXX American Chemical Society

DOI: 10.1021/acs.inorgchem.5b00157
Inorg. Chem. XXXX, XXX, XXX−XXX

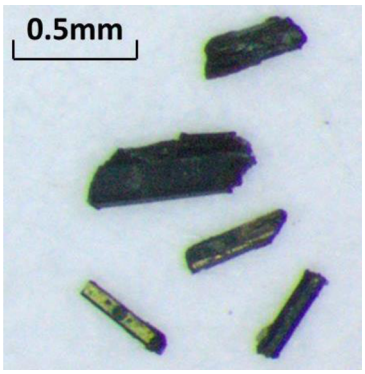

Figure 1. Representative single crystals of $Ba_8Al_2IrO_{14}$.

numbers the low EDX efficiency for the light element Al must be taken into account.

Structure Determination. Single-crystal X-ray diffraction (XRD) data were measured at room temperature and low temperature (90 K) using Mo Kα radiation on a Bruker APEX II CCD diffractometer equipped with a kappa geometry goniometer. The data set was reduced by EvalCCD and then corrected for absorption.[14,15] The solution and refinement were performed by SHELX.[16,17] The crystal structure was refined using full-matrix least-squares based on F^2.

Transport Measurements. Resistivity ρ was measured by a standard four-probe method in the 180−600 K temperature range. Evaporation of chromium/gold contacts on the crystal surface was performed to reduce the contact resistance. To measure Seebeck coefficient S the sample was placed on a ceramic bar, at one end of which a small heater was anchored to generate heat, which was sent through the crystal. The temperature gradient across the specimen was measured by a differential Chromel−Constantan thermocouple. The Seebeck coefficient was evaluated in the 300−680 K temperature range due to the high resistance of our crystal.

Optical Measurements. Optical measurements were performed at room temperature. Transmission and reflectivity were measured in the range from 0.15 to 0.5 eV and complemented by spectroscopic ellipsometry from 0.5 to 2.6 eV.

Magnetization Measurements. The magnetic susceptibility $\chi(T) = M(T)/H$ at constant H was measured using a superconducting quantum interference device (SQUID) magnetometer in the 2−300 K temperature range with H = 0.1, 1, and 5 T applied both parallel and perpendicular to the b-axis employing both zero-field cooling (ZFC) and field-cooling (FC) protocols. The isothermal magnetization $M(H)$ was measured for T = 2, 5, and 10 K in fields up to H = 5 T. Measurements were made on an aligned stack of dozens of needles with a total mass of 7.0 mg. All b-axis coincided, whereas measurements with $H \perp b$ hence measure an average over direction perpendicular to b-axis.

RESULTS AND DISCUSSION

Crystal Structure. According to the systematic absences of the XRD reflections, the space groups $C2/m$, Cm, and $C2$ can be suggested. The structure refinements were performed for all these space groups and finalized with nearly the same reliability factor $R_1 \approx 4\%$. Therefore, the highest symmetric space group, $C2/m$ (No.12) was selected.

The lattice parameters were determined as a = 19.8367(14), b = 5.9709(6), c = 7.6138(7) Å, $\alpha = \gamma = 90°$, and β = 109.785(5)°. The longest size of the needlelike crystals coincides with the b-axis. Further details of the data collection, structure determination, and refinement are listed in Tables 1 and 2. The crystal structure of $Ba_8Al_2IrO_{14}$ is shown in Figure 2, where the IrO_6 octahedra and AlO_4 tetrahedra are outlined.

The crystal structure of $Ba_8Al_2IrO_{14}$ is related to $Sr_8Si_2PtO_{14}$, reported in ref 18 with asymmetric space group $C2$ (No. 5), a = 18.830(2), b = 5.744(1), c = 7.172(1) Å, and β = 110.72(1)°. Both structures contain identical number, 50, of atoms per similar unit cell, and they can be described with the same type of cationic polyhedra (Figure 2). Isolated AlO_4 tetrahedra (SiO_4 in $Sr_8Si_2PtO_{14}$) and IrO_6 octahedra (PtO_6 in $Sr_8Si_2PtO_{14}$) are separated by Ba ions (Sr ions in $Sr_8Si_2PtO_{14}$). The IrO_6 octahedra are slightly distorted with two 2.041(7) Å long and four 1.970(5) Å short Ir−O distances (Table 2). The structure refinement yields very large anisotropic displacement parameters (ADP) for one oxygen atom, O5a, in the AlO_4 tetrahedra (inset of Figure 2). A reduced occupancy of the O5a site is unreasonable because the Al tetrahedron is a strong unit from which it is highly unlikely that an oxygen can be removed. Furthermore, allowing reduced occupancy on this site in the refinement does not remove the large elongation of the ADP ellipsoid. Anharmonic atomic displacement of O5a was also excluded because no reduction of its atomic displacements can be observed in the structure obtained at 90 K. We therefore conclude that rather than thermal motion, this oxygen is split between two nearby positions, O5a and O5b (Figure 2). The splitting of O5a and O5b can also be explained from the consideration of the first coordination spheres of Ba3 and Al1 (Table 2). Two positions of O5a are necessary to form Ba3 octahedron with 2.5755(6) Å short distances between Ba3 and O5a, while the O5b positions cannot compensate a charge Ba due to the 3.1308(7) Å long distances between Ba3 and O5b. On the other hand, two O5b positions are necessary to form Al1-tetrahedron with 1.628(3) Å short distances between Al1 and O5b, while the O5a is too far from Al1 (with 1.8740(13) Å long distances between Al1 and O5a). Therefore, statistical

Table 1. Details of the Data Collection and Structure Refinement for $Ba_8Al_2IrO_{14}$[a]

empirical formula	$Ba_8Al_2IrO_{14}$	
formula weight (g/mol)	1568.88	
temperature (K)	293(2)	90(2)
unit cell dimensions (Å, deg)	a = 19.8367(14), b = 5.9709 (6)	a = 19.8283(15), b = 5.9591(5)
	c = 7.6138(7); β = 109.785 (5)	c = 7.6013(5); β = 109.656(5)
volume (Å^3)	848.57(13)	845.82(11)
calculated density (g/cm^3)	6.140	6.160
absorption coefficient (mm^{-1})	26.212	26.297
F(000)	1326	
θ range for data collection (deg)	3.58−34.98	3.59−35.00
index ranges	$-32 \le h \le 30$, $-9 \le k \le 9$, $-12 \le l \le 12$	
reflections collected/ unique	10 716/2019 $R_{int.}$= 0.0564	12095/2014 $R_{int.}$= 0.0537
completeness to 2θ	99.8%	99.8%
data/restraints/ parameters	2019/0/64	2014/0/64
goodness-of-fit on F^2	1.133	1.110
final R indices [$I > 2\sigma(I)$]	R_1 = 0.0390, wR_2 = 0.0918	R_1 = 0.0392, wR_2 = 0.0791
R indices (all data)	R_1 = 0.0442, wR_2 = 0.0949	R_1 = 0.0455, wR_2 = 0.0821

[a]The diffraction study was performed at 293(2) and 90(2) K using Mo Kα radiation with λ = 0.710 73 Å. The lattice is monoclinic, $C2/m$ space group, with Z = 2. A full-matrix least-squares method was employed to optimize F^2.

DOI: 10.1021/acs.inorgchem.5b00157
Inorg. Chem. XXXX, XXX, XXX−XXX

Table 2. Selected Interatomic Distances (Å) for $Ba_8Al_2IrO_{14}$

atom$_1$	atom$_2$	count	d 1,2 [Å]	atom$_1$	atom$_2$	count	d 1,2 [Å]
Ir1	O3	4×	1.970(5)	Ba3	O4	1×	2.924(12)
	O2	2×	2.041(7)		O4	2×	3.0196(18)
Ba1	O1	1×	2.739(13)		O5b	2×	3.1308(7)
	O4	1×	2.750(11)	Ba4	O5a	2×	2.5755(7)
	O1	1×	2.750(11)		O2	1×	2.610(8)
	O3	2×	2.767(5)		O3	2×	2.813(5)
	O3	2×	2.868(5)		O5b	2×	2.8676(6)
	O2	2×	2.9960(7)		O1	2×	3.040(2)
Ba2	O5b	2×	2.5396(5)		O2	1×	3.052(7)
	O5a	2×	2.6044(5)	Al1	O5b	2×	1.628(3)
	O4	1×	2.698(12)		O4	1×	1.724(12)
	O3	2×	2.712(5)		O1	1×	1.707(13)
	O5b	2×	2.9292(6)		O5a	2×	1.8740(13)
	O1	1×	2.995(13)	O5a	O5b	1×	0.8292(1)
Ba3	O5a	2×	2.5755(6)	Ir1	Ba4	2×	3.3884(8)
	O2	1×	2.686(8)		Ba3	2×	3.4534(7)
	O3	2×	2.863(5)		Ba1	2×	3.4913(4)

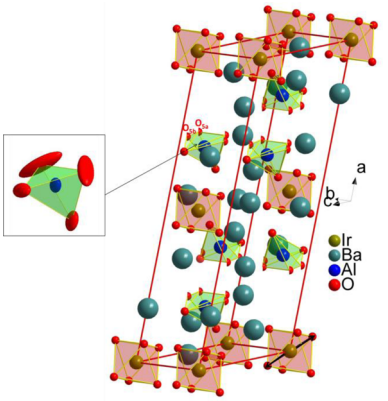

Figure 2. Crystal structure of $Ba_8Al_2IrO_{14}$. Red and green polyhedral indicate IrO_6 octahedra and AlO_4 tetrahedra, respectively. The black arrows mark the long axis direction of the elongated octahedra. The unit cell is outlined in red. (inset) AlO_4 tetrahedron with the extremely large ADP ellipsoid of nonsplit oxygen atom with atomic displacement ellipsoids at 50% probability. Splitted atoms, O5a and O5b, are shown with half spheres indicating their occupation of 50%.

occupation of O5a and O5b is a solution of the situation. Refinements allowing a variable occupancy on O2 and O3 in the IrO_6 octahedra yielded 100% (Table 3).

The oxidation state of metal ions in solids may be estimated using an empirical quantity, known as the bond valence sum (BVS), which is based on statistics of crystallographically determined metal−ligand bond distance. V_i, the effective valence or BVS of the ith atom, is determined by

$$V_i = \sum_j S_{ij} = \sum_j \exp[(r_0 - r_{ij})/0.37] \quad (1)$$

where r_0 is empirically determined for each i−j atomic pair, and r_{ij} is the observed interatomic distance between the ith and jth atom in the material under consideration. S_{ij} can be considered to be the effective charge in the r_{ij} bond. V_i is then obtained as the sum over j of all of the S_{ij}. Reference 13 reported two all-Ir^{6+} containing oxides, namely, $Nd_2K_2IrO_7$ (Ir−O distance 1.982 Å) and $Sm_2K_2IrO_7$ (Ir−O distance 1.972 Å), prepared under ambient pressure. Using these two compounds the average r_0 for Ir^{6+}−O is 1.977 Å. For $Ba_8Al_2IrO_{14}$, the four 1.970 Å bonds and the two 2.041 Å bonds (Table 2) give a BVS of 5.76(9) for Ir, suggesting that Ir(VI) is the most likely oxidation state—in agreement with the stoichiometry obtained from crystallography.

Transport Properties. The electrical resistivity ρ of $Ba_8Al_2IrO_{14}$ measured in the 180−600 K temperature range is shown in Figure 3a. The resistivity value is 7.3 kΩ cm at room temperature, and ρ increases monotonically as temperature decreases ($d\rho/dT < 0$), revealing the insulating nature of this compound. In the inset of Figure 3a, we show $d(\ln\rho)/d(e/k_BT)$ versus T. Thermally activated behavior is observed above 350 K. In this temperature range $\rho(T)$ can be described by the formula

$$\rho(T) = \rho_0 \exp(E_a/k_BT) \quad (2)$$

where ρ_0 is a parameter depending on the sample characteristics, k_B is Boltzmann's constant, T is absolute temperature, and E_a denotes the thermal activation energy of electrical conduction. It yielded the activation energy E_a = 0.290 eV ± 0.005 eV. In this case, a rough estimate of band gap energy $E_g = 2E_a$ is 0.58 eV ± 0.01 eV above 350 K. At lower temperature, the resistivity deviates from activated behavior.

As shown in Figure 3b, the Seebeck coefficient S of $Ba_8Al_2IrO_{14}$ is positive in the whole temperature range, suggesting hole-dominated conduction. At room temperature, S = 7500 μV/K. S further decreases with temperature increasing, as expected for insulators, and changes gradually with no clear transition temperature in the temperature range of 300−500 K and 620−680 K.

Table 3. Atomic Occupancy for $Ba_8Al_2IrO_{14}$

Ir1	Ba1	Ba2	Ba3	Ba4	Al1	O1	O2	O3	O4	O5a	O5b
1	1.006(2)	1.007(2)	1.011(2)	1.001(3)	0.974(11)	0.99(2)	1.03(2)	1.031(14)	1.02(3)	0.46(2)	0.51(2)

DOI: 10.1021/acs.inorgchem.5b00157
Inorg. Chem. XXXX, XXX, XXX−XXX

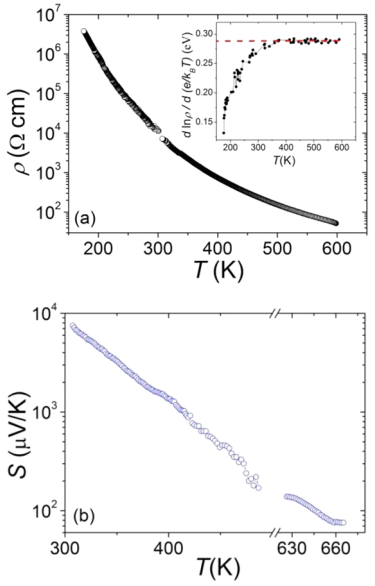

Figure 3. (a) Electrical resistivity of $Ba_8Al_2IrO_{14}$. (inset) $d(\ln\rho)/d(e/k_BT)$ vs T. The red dashed line is the guide to eyes of this fitting. $E_a \approx 0.29$ eV is estimated above 350 K in this plot. (b) The temperature dependence of the Seebeck coefficient of $Ba_8Al_2IrO_{14}$.

Optical Properties. The optical transmission and reflectivity are shown in Figure 4a from 0.15 to 0.5 eV at room temperature. The low reflectivity and the high transmission indicate the insulating behavior in this material. These two quantities are related to the dielectric function $\varepsilon = \varepsilon_1 + i\varepsilon_2$. Figure 4b shows the real and imaginary part of the dielectric function, ε_1 and ε_2, as determined by the ellipsometry from 0.5 to 2.6 eV. By simultaneously fitting the above optical quantities, one obtains an estimate of the complex dielectric function ε, and from it the real part of the optical conductivity, $\sigma_1(\omega)$, is shown in Figure 4c. The conductivity $\sigma_1(\omega)$ is gapped below ~0.7 eV, indicating the insulating behavior of this material, which is in accordance with the results of resistivity. Below the gap, several sharp oscillations are seen, which can be attributed to vibrational phonon modes. Two strong absorptions can be seen above the gap, centered at 1.2 and 2.2 eV, which are likely intraband transitions.

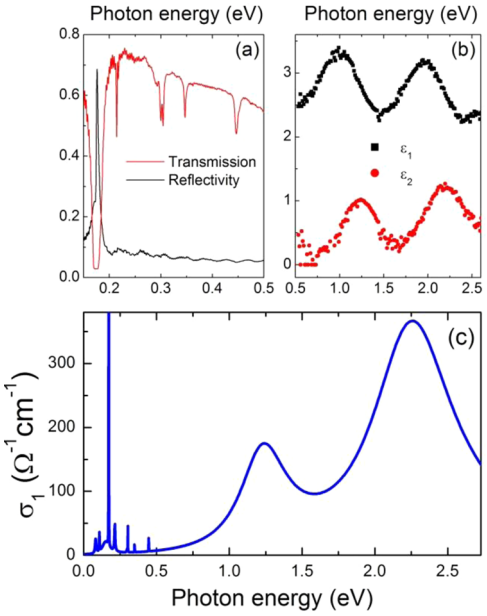

Figure 4. (a) Transmission and reflectivity spectra as a function of photon energy for $Ba_8Al_2IrO_{14}$ at room temperature. (b) The real and imaginary part of the dielectric function. (c) The real part of optical conductivity, $\sigma_1(\omega)$, modeled from the transmission, reflectivity, and ellipsometry data, shown at 300 K.

Magnetic Properties. The temperature dependence of magnetic susceptibility parallel to the b-axis of $Ba_8Al_2IrO_{14}$, measured in applied magnetic fields of 0.1, 1, and 5 T, is shown in Figure 5a. The susceptibility increases monotonically with decreasing temperature and shows no indication of long-range order. The zero-field cooling (ZFC) and field-cooling (FC) data completely overlay at all temperatures down to 2 K. The susceptibilities that are, respectively, parallel and perpendicular to the b-axis are compared in Figure 5b, showing the magnetic anisotropy of $Ba_8Al_2IrO_{14}$.

To analyze the T dependence of the anisotropic susceptibility quantitatively, we plotted $(M/H)_\perp$ (T) versus $(M/H)_\parallel$ (T) with an implicit parameter T in the inset of Figure 5b. The analysis mentioned in ref 19 leads to the relation between $\chi_\parallel(T)$ and $\chi_\perp(T)$:

$$\chi_\perp(T) = (g_\perp/g_\parallel)^2\chi_\parallel(T) + [\chi_0^\perp - (g_\perp/g_\parallel)^2\chi_0^\parallel] \quad (3)$$

The main point of this analysis is that the fitted slope of the data corresponds to the ratio $(g_\perp/g_\parallel)^2$. $Ba_8Al_2IrO_{14}$ has the anisotropy of $(g_\perp/g_\parallel)^2 = 0.50(5)$.

Further fitting the data above 50 K to a modified Curie–Weiss (CW) law

$$\chi(T) = C/(T - \theta) + \chi_0 \quad (4)$$

yielded a Curie–Weiss constant $C = 0.23(1)$ emu/(mol K), an effective moment $\mu_{eff} = 1.36(3)$ μ_B per formula unit, a Curie temperature $\theta = -10(1)$ K and a temperature independent term $\chi_0 = 1.15 \times 10^{-3}$ emu/mol for $H \parallel b$ (parallel to the needle direction) and $C = 0.16(1)$ emu/(mol K), $\mu_{eff} = 1.13(4)$ μ_B per formula unit, $\theta = -32(2)$ K and $\chi_0 = 2.59 \times 10^{-3}$ emu/mol for $H \perp b$ (perpendicular to the needle direction).

The negative Curie temperature θ indicates antiferromagnetic (AFM) coupling. The anisotropy obtained from Curie–Weiss fitting is $(\mu_{eff_\perp}/\mu_{eff_\parallel})^2 = 0.69(8)$, which is in same direction but numerically different from the $(g_\perp/g_\parallel)^2 = 0.50(5)$ in the plot of $(M/H)_\perp(T)$ versus $(M/H)_\parallel(T)$. This is because the latter assumes same functional form for $(M/H)_\perp(T)$ and $(M/H)_\parallel(T)$, which is not the case if θ is anisotropic. The anisotropic Curie–Weiss constant C indicates the magnetic anisotropy of this compound, which can be understood from an anisotropic g-factor, as we discussed before. The temperature independent term χ_0 is rather large and anisotropic, but similar large and anisotropic valuhas been reported for other compounds, such as $NaIrO_3$, $Pr_2Ir_2O_7$ and $Na_xCoO_2 \cdot yH_2O$.[19−21]

The Ir^{6+} ions sit in an octahedral crystal field generated by the neighboring O^{2-} ions splitting the 5d orbitals into higher e_g and lower t_{2g} levels. The electronic configuration of the Ir^{6+} being $5d^3$ the t_{2g} crystal field levels are half occupied, and the Hund coupling selects the high-spin $S = 3/2$ state. However, the effective moment for a spin-3/2 isotropic paramagnet is $\mu_{eff} = 3.87$ μ_B far larger than the observed $\mu_{eff} = 1.36$ μ_B. The strong SOC present in the Ir 5d orbitals ($\lambda_{SO} \approx 400$ meV) has been shown to lead to such a reduction of the $5d^3$ effective magnetic

DOI: 10.1021/acs.inorgchem.5b00157
Inorg. Chem. XXXX, XXX, XXX−XXX

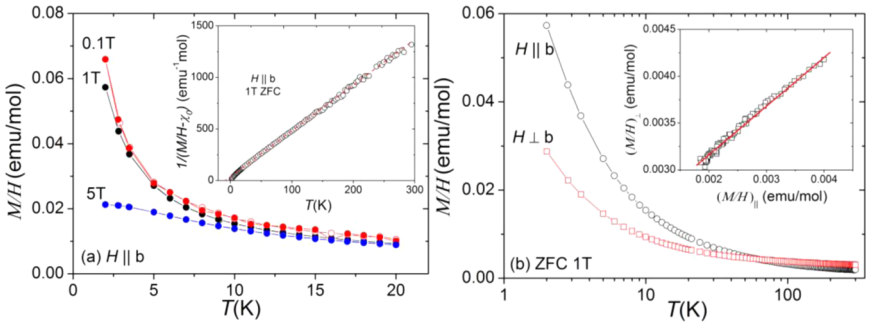

Figure 5. (a) Temperature dependence of M/H, which approximates the magnetic susceptibility except below 10 K where $M(T)$ starts to deviate from linearity of $Ba_8Al_2IrO_{14}$ under various fields applied parallel to the b-axis. Both ZFC and FC data are shown. (inset) Inverse magnetic susceptibility $1/(M/H - \chi_0)$ versus temperature T in a magnetic field H = 1 T (ZFC). (b) Temperature-dependent magnetic susceptibility of $Ba_8Al_2IrO_{14}$ under H = 1 T applied perpendicular and parallel to the b-axis, respectively, in ZFC. (inset) (M/H) versus (M/H).

moment, while the tetragonal distortion of the octahedron will further reduce it.[22−24] Comparing the measured effective moment with the one for an isotropic $S = 3/2$ paramagnet, we have for $H \parallel b$

$$\mu_{\text{eff}} = g\sqrt{S(S+1)}\,\mu_B = 1.36\mu_B \quad (5)$$

yielding a reduced g-factor $g_{\parallel} = 0.58$.

The magnetic field dependence H applied parallel to the b-axis of the magnetization of $Ba_8Al_2IrO_{14}$, measured at different temperatures, is shown in Figure 6. The dashed lines are

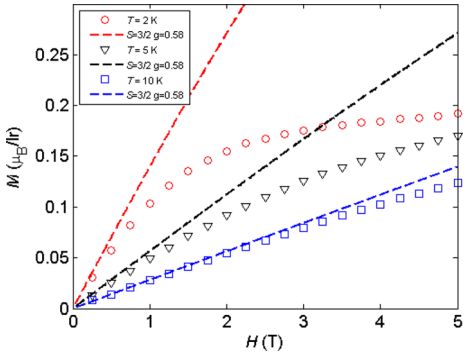

Figure 6. Isothermal magnetization M versus magnetic field H applied parallel to the b-axis at various temperatures T. The dashed lines are fits to the Brillouin functions for $S = 3/2$, $g = 0.58$.

Brillouin functions for $S = 3/2$, $g = 0.58$. The $M(H)$ data above T = 10 K follow the Brillouin function, indicating the absence of any ferromagnetic impurities in the material. At lower T, $M(H)$ values become gradually smaller than the Brillouin function, indicating dominant antiferromagnetic coupling.

CONCLUSIONS

We synthesized a new compound $Ba_8Al_2IrO_{14}$ and systematically studied its crystal structure and transport, optical, and magnetic properties. It has been prepared as single crystals by self-flux method, thereby providing a rare example of an all-Ir(VI) compound that can be synthesized under ambient pressure conditions. Our experiment shows $Ba_8Al_2IrO_{14}$ has monoclinic crystal structure with the space group of $C2/m$ (12). It is a p-type band insulator with a narrow band gap of ~0.6 eV, and these are confirmed by the optical measurements. Furthermore, $Ba_8Al_2IrO_{14}$ shows antiferromagnetic couplings but displays no order down to 2 K. We hope this work will stimulate more investigations on these Ir-based materials that offer a wide window into the research of spin−orbit interactions and the strength of electronic correlations.

ASSOCIATED CONTENT

Supporting Information

Crystallographic files in CIF format for $Ba_8Al_2IrO_{14}$. This material is available free of charge via the Internet at http://pubs.acs.org.

AUTHOR INFORMATION

Corresponding Author

*E-mail: henrik.ronnow@epfl.ch.

Notes

The authors declare no competing financial interest.

ACKNOWLEDGMENTS

We gratefully thank F. M. Mor for help with crystal structure analysis, and P. Huang and P. Babkevich for discussions concerning the magnetic properties. This work was supported by the Swiss National Science Foundation and its Sinergia Network Mott Physics Beyond the Heisenberg model (MPBH).

REFERENCES

(1) Cao, G.; Xin, Y.; Alexander, C. S.; Crow, J. E.; Schlottmann, P.; Crawford, M. K.; Harlow, R. L.; Marshall, W. *Phys. Rev. B* **2002**, *66*, 214412.
(2) Singh, Y.; Gegenwart, P. *Phys. Rev. B* **2010**, *82*, 064412.
(3) Erickson, A. S.; Misra, S.; Miller, G. J.; Gupta, R. R.; Schlesinger, Z.; Harrison, W. A.; Kim, J. M.; Fisher, I. R. *Phys. Rev. Lett.* **2007**, *99*, 016404.
(4) Yang, B. J.; Kim, Y. B. *Phys.Rev.B* **2010**, *82*, 085111.
(5) Pesin, D. A.; Balents, L. *Nat. Phys.* **2010**, *6*, 376−381.
(6) Wang, F.; Senthil, T. *Phys. Rev. Lett.* **2011**, *106*, 136402.
(7) Dey, T.; Panda, S. K.; Mahajan, A. V.; Dasgupta, I.; Koteswararao, B.; Chou, F. C.; Omrani, A. A.; Ronnow, H. M. *arXiv:1210.4355v1*; Cornell University Library, 2012. Online: http://xxx.tau.ac.il/abs/1210.4355v1.
(8) Jung, D. Y.; Demazeau, G.; Etourneau, J.; Subramanian, M. A. *Mater. Res. Bull.* **1995**, *30*, 113−123.
(9) Jung, D. Y.; Gravereau, P.; Demazeau, G. *Eur. J. Solid State Inorg. Chem.* **1993**, *30*, 1025−1037.
(10) Demazeau, G.; Jung, D. Y.; Sanchez, J. P.; Colineau, E.; Blaise, A.; Fournes, L. *Solid State Commun.* **1993**, *85*, 479−484.
(11) Choy, J. H.; Kim, D. K.; Hwang, S. H.; Demazeau, G.; Jung, D. Y. *J. Am. Chem. Soc.* **1995**, *117*, 8557−8566.

DOI: 10.1021/acs.inorgchem.5b00157
Inorg. Chem. XXXX, XXX, XXX−XXX

(12) Park, J.; Park, J. G.; Swainson, I. P.; Ri, H. C.; Choi, Y. N.; Lee, C.; Jung, D. Y. *J. Korean Phys. Soc.* **2002**, *41*, 118−122.
(13) Mugavero, S. J.; Smith, M. D.; Yoon, W. S.; Loye, H. C. *Angew. Chem., Int. Ed. Engl.* **2009**, *48*, 215−218.
(14) Duisenberg, A. J. M.; Kroon-Batenburg, L. M. J.; Schreurs, A. M. M. *J. Appl. Crystallogr.* **2003**, *36*, 220−229.
(15) Blessing, R. H. *Acta Crystallogr., Sect. A* **1995**, *51*, 33−38.
(16) Sheldrick, G. M. *Acta Crystallogr., Sect. A* **2008**, *64*, 112−122.
(17) Sheldrick, G. M. *SHELXL-97—Program for the Refinement of Crystal Structures;* University of Gottingen: Goettingen, Germany, 1997.
(18) Stenberg, L. *Acta Crystallogr., Sect. C* **1988**, *44*, 955−957.
(19) Chou, F. C.; Cho, J. H.; Lee, Y. S. *Phys. Rev. B* **2004**, *70*, 144526.
(20) Bremholm, M.; Dutton, S. E.; Stephens, P. W.; Cava, R. J. *J. Solid State Chem.* **2011**, *184*, 601−607.
(21) Machida, Y.; Nakatsuji, S.; Tonomura, H.; Tayama, T.; Sakakibara, T.; Duijn, J.; van Broholm, C.; Maeno, Y. *J. Phys. Chem. Solids* **2005**, *66*, 1435−1437.
(22) Kim, B. J.; Jin, H.; Moon, S. J.; Kim, J.-Y.; Park, B.-G.; Leem, C. S.; Yu, J.; Noh, T. W.; Kim, C.; Oh, S.-J.; Park, J.-H.; Durairaj, V.; Cao, G.; Rotenberg, E. *Phys. Rev. Lett.* **2008**, *101*, 076402.
(23) Matsuura, H.; Miyake, K. *J. Phys. Soc. Jpn.* **2013**, *82*, 073703.
(24) Boča, R. *Struct. Bonding (Berlin, Ger.)* **2006**, *117*, 1−264.

DOI: 10.1021/acs.inorgchem.5b00157
Inorg. Chem. XXXX, XXX, XXX−XXX